The Astrophysical Journal, 876:120 (14pp), 2019 May 10 https://doi.org/10.3847/1538-4357/ab16f0

Analysis of Meteoroid Ablation Based on Plasma Wind-tunnel Experiments, Surface Characterization, and Numerical Simulations

Bernd Helber[1], Bruno Dias[1,2], Federico Bariselli[1,3,4], Luiza F. Zavalan[1], Lidia Pittarello[5], Steven Goderis[6], Bastien Soens[6], Seann J. McKibbin[6,7,8], Philippe Claeys[6], and Thierry E. Magin[1]
[1] Aeronautics and Aerospace Department, von Karman Institute for Fluid Dynamics, Rhode-Saint-Genèse, Belgium; helber@vki.ac.be
[2] Institute of Mechanics, Materials and Civil Engineering, Université catholique de Louvain, Louvain-la-Neuve, Belgium
[3] Research Group Electrochemical and Surface Engineering, Vrije Universiteit Brussel, Brussels, Belgium
[4] Dipartimento di Scienze e Tecnologie Aerospaziali, Politecnico di Milano, Milano, Italy
[5] Department of Lithospheric Research, University of Vienna, Vienna, Austria; lidia.pittarello@univie.ac.at
[6] Analytical, Environmental, and Geo-Chemistry, Vrije Universiteit Brussel, Brussels, Belgium
[7] Institute of Earth and Environmental Science, University of Potsdam, Potsdam-Golm, Germany
[8] Geowissenschaftliches Zentrum, Georg-August-Universität Göttingen, Göttingen, Germany
Received 2018 November 28; revised 2019 April 5; accepted 2019 April 5; published 2019 May 10

Abstract

Meteoroids largely disintegrate during their entry into the atmosphere, contributing significantly to the input of cosmic material to Earth. Yet, their atmospheric entry is not well understood. Experimental studies on meteoroid material degradation in high-enthalpy facilities are scarce and when the material is recovered after testing, it rarely provides sufficient quantitative data for the validation of simulation tools. In this work, we investigate the thermo-chemical degradation mechanism of a meteorite in a high-enthalpy ground facility able to reproduce atmospheric entry conditions. A testing methodology involving measurement techniques previously used for the characterization of thermal protection systems for spacecraft is adapted for the investigation of ablation of alkali basalt (employed here as meteorite analog) and ordinary chondrite samples. Both materials are exposed to a cold-wall stagnation point heat flux of 1.2 MW m^{-2}. Numerous local pockets that formed on the surface of the samples by the emergence of gas bubbles reveal the frothing phenomenon characteristic of material degradation. Time-resolved optical emission spectroscopy data of ablated species allow us to identify the main radiating atoms and ions of potassium, calcium, magnesium, and iron. Surface temperature measurements provide maximum values of 2280 K for the basalt and 2360 K for the chondrite samples. We also develop a material response model by solving the heat conduction equation and accounting for evaporation and oxidation reaction processes in a 1D Cartesian domain. The simulation results are in good agreement with the data collected during the experiments, highlighting the importance of iron oxidation to the material degradation.

Key words: meteorites, meteors, meteoroids – plasmas – techniques: spectroscopic

1. Introduction

Meteoroids provide our primary source of extraterrestrial materials from the various nebular and planetary environments of the solar system and beyond. These naturally delivered samples, bringing in 50–100 tons of material every day (Flynn 2002), undergo melting and evaporation during their entry into the Earth's atmosphere. This results in variable levels of modification that need to be distinguished from pre-entry features in order to understand processes occurring during transport in open space, residence in or on their parent body, and ultimately their original formation during the earliest history of the solar system.

Among the daily material delivered to our planet, the Chelyabinsk event in 2013 (Brown et al. 2013) renewed awareness of potential hazards, motivating the planning of deflection and mitigation strategies of incoming asteroids (Prabhu et al. 2015). These strategies rely on knowledge of the physical properties of the material and structure of the incoming object. Space agencies launched sample–return missions to asteroids such as Hayabusa II (Vilas 2008), and to comets such as 67P/Churyumov–Gerasimenko (Taylor et al. 2017) to collect data relevant to their formation and composition. The complexity and operational costs of these missions motivated scientists to study the meteor phenomenon as a bridge between meteorites and their parent bodies.

Our knowledge of this phenomenon mainly relies on geochemical characterization of the samples that survived entry and were collected on the ground, or on visual observations, such as radar and radio detection (Martínez Picar et al. 2016). The interpretation of these data derives from models that correlate the plasma signature to a signal from which the size, velocity, and composition of the body are inferred. On the other hand, chemical inspection of meteorites provides information only about the final outcome of the trajectory without the possibility to understand which conditions these features are related to. Ground experiments provide an opportunity to look at the meteor phenomenon in detail, with the possibility of focusing on the gas–surface interaction for well-defined flight conditions and material properties, which remain poorly understood. The goal of this work is to contribute to a better understanding of the gas–surface interaction processes during a meteoroid entry with new plasma wind-tunnel experimental data, surface characterization, and numerical simulations, leading to the development of thermo-chemical ablation models.

Validation of models through ground experiments is part of the margin analysis for thermal protection systems (TPSs), which protect the astronauts and payload from severe heat loads to the spacecraft during its re-entry. Although different in nature (e.g., the silicate melt can be removed from the body due to aerodynamic forces), meteoroids present many similarities with TPSs and they can be studied taking advantage of the well established techniques in the field of heat shield characterization.

The first wave of ground experiments for meteor studies dates back to the middle of the 20th century. Thomas & White (1953) compared the atomic spectra of observed meteors with those obtained by ultra-speed pallets in a ballistic facility. Almost 10 years later, the interaction between a hypersonic flow and an axial symmetric ablator was investigated by Zotikov (1962) by ensuring that the stagnation temperature of the flow exceeded the melting temperature of the body. The process of ablation was observed visually and photographed with a motion picture camera. Attention was paid to the shape and form of the samples after ablation. As a result, general laws of the process of body ablation were obtained, as well as quantitative data on heat transfer in the range of parameters of the experiment.

The first experiments in an Arcjet facility at NASA Ames Research Center were performed by Shepard et al. (1967) who compared the luminous intensity of meteorite analogues such as gabbro and basalt with stony meteorites. The authors observed similar intensities from artificial and natural meteorites, proposing the use of artificial samples to gain better knowledge on the ablation of asteroidal meteors. Using the same facility, Allen & Baldwin (1967) studied the effective density variation of potential cometary-type meteors due to the frothing phenomenon. These types of meteors are expected to include a high water content, which evaporates when certain conditions are reached, resulting in a density anomaly. Bronshten (1983) conducted experiments on samples of stony and iron meteorites in an inductively coupled plasma (ICP) facility. After an initial stage during which the sample warmed up, softened, and liquefied, the sample started to ablate. From the observations, it was possible to infer that melting and mechanical disintegration were probably dominant at altitudes lower than 100 km, with the direct vaporization of material dominating only above 120 km. As the author admitted, however, it is questionable that the mentioned experiments had been able to replicate the extreme environment taking place during hypervelocity atmospheric entry, with realistic surface temperatures and heat fluxes. A series of experimental studies on ablation were also conducted by Blanchard & Cunningham (1974). Experiments on a meteorite analog, olivine, showed a similar fusion crust and oxidation level as the recovered carbonaceous chondrite meteorites. The authors pointed out that the elemental and mineralogical composition as well as the morphological and textural features must be taken into account.

More recently, two series of experiments were performed making use of improved measurement and inspection techniques. Loehle et al. (2017) tested an H4 chondrite and analog samples at the Institut für Raumfahrtsysteme (IRS) with the objective of gaining a better understanding of the ablation process and associated spectral features. Cylindrical-shaped samples were exposed to high heat flux until complete disintegration. The spectra measured by Echelle spectroscopy gave a good comparison with flight data. The surface quickly reached a constant temperature at around 2400 K. In the work by Agrawal et al. (2018), the extreme entry conditions experienced by the Chelyabinsk meteorite during its entry were reproduced. Two samples of the H5 Tamdakht chondrite and one iron meteorite, all carved into a spherical cone shape, were exposed for few seconds to a plasma flow in the Arcjet Interaction Heating Facility of NASA Ames. The chondrite resisted for 2 s while the iron meteorite was completely destroyed after 2.5 s. For all samples, substantial removal of the melt by shearing effects was observed and values for the effective heat of ablation were derived, leading to an improvement of the current models.

In parallel to the experiments in high-enthalpy facilities, intensive evaporation has been studied by directing a high-power laser beam toward the surface of meteorite test samples. This type of experiment is designed to reproduce the strong heating rate on the surface upon the entry of a bolide at high velocities. Milley et al. (2007) investigated the production of light during meteor ablation to better estimate the luminosity efficiency. The expanding vapor was observed by charge-coupled device (CCD) detectors used for meteor observations. The spectral features contained mainly neutral atoms and light production from the vapor was observed even in the absence of high-speed collisions with air constituents. The same technique was used to study the thermo-chemical behavior of the material when subjected to high heat fluxes (White & Stern 2017). Ferus et al. (2018) developed a methodology to analyze and interpret real-time plasma spectra from meteor detections using a calibration-free method. The method was validated by comparison with laboratory experiments in which measurements, performed using laser-induced breakdown spectroscopy, allowed quantitative determination of elemental compositions and temperatures in Perseid and Leonid events.

In the work of Bones et al. (2016), a novel facility (the Meteoric Ablation Simulator) was presented to study differential evaporation in interplanetary dust particles ($<50\ \mu$m) in free-molecular flow. The authors were able to produce a controlled heating rate to represent entry conditions and to measure impact ionization coefficients for the interpretation of radio and radar observations. Gómez Martín et al. (2017) observed differential ablation effects, showing that sodium is the major contributor for radio observation due to its high volatility and low ionization energy.

Experimental replication of meteor entry in a clean plasma flow is a challenging procedure. For instance, the main disadvantage of Arcjet facilities is the presence of copper in the flow due to cathode erosion and degradation, possibly catalyzing surface reactions (Hardy & Nakanishi 1984). Furthermore, although laser ablation guarantees high heat fluxes and is suitable for detailed analysis of gas–surface interactions thanks to the controlled environment, it essentially fails in reproducing the highly reactive plasma around the material, which is generated by the entry shock wave. Moreover, understanding of the ablation process requires surface temperature measurements, spectral features of the evaporating gases, visual observation of the surface, and sample recovery for a posteriori material analysis.

In this paper, we present the results from an experimental campaign using an ICP wind-tunnel (Plasmatron), which took place at the von Karman Institute for Fluid Dynamics (VKI) (Table 1). The subsonic 1.2 MW Plasmatron facility is able to reproduce the aerothermodynamic environment of atmospheric entry in the boundary layer of a test object for a wide range of pressures and heat fluxes (Bottin 1999; Bottin et al. 1999). The focus of our study is the characterization of the gas–surface interaction processes occurring during meteoroid entry. We propose to employ experimental diagnostic techniques previously developed for the in situ material response

Table 1
Comparison of Recent Meteoroid Ablation Test Campaigns in Different High-enthalpy Facilities

Facility	p_s (hPa)	$\dot{q}_{cw}$ (MW m^{-2})	h_e (MJ kg^{-1})	Configuration	Reference
VKI Plasmatron	15–200	1–3	24–54	Stagnation point	Present study
IRS Arcjet	24	16	70	Cylindrical sample	Loehle et al. (2017)
Ames Arcjet	14	40	20	Full axisymmetric body	Agrawal et al. (2018)

characterization of heat shield materials (Helber et al. 2016a), with the objectives to record the surface temperature evolution, visually observe the ablation process, and recover tested samples for their comparison with fusion crusts on natural meteorites (Pittarello et al. 2019). In addition, three emission spectrometers are focused on the boundary layer forming in front of the ablating material, providing temporally resolved emission profiles of the main radiators ejected by the test sample during the entire test time. The retrieved data are then used to build a thermal response model of the material by solving the heat conduction equation in a 1D Cartesian domain, which provides a more detailed insight into the surface energy balance and chemical reaction of iron oxidation. Two types of materials are studied, alkali basalt (AB), as a meteorite analog to optimize the experimental conditions, and ordinary chondrite (OC), with the main focus on the temperature response, surface characterization, and gas-phase radiation.

We describe the methodology and experimental facility in Section 2. Section 3 deals with the testing conditions. After sketching the theory, the similarity rules are applied to rebuild flight conditions from the experiment. Section 4 presents the experimental results obtained in this work: after a qualitative analysis, surface measurements and emission spectra are shown and discussed. Finally, in Section 5, the surface measurements are compared with simulations results obtained by means of the material response code.

2. Experimental Facility, Measurement Techniques, and Methods

The experimental setup installed at the Plasmatron facility offers intrusive and non-intrusive (optical) measurement techniques. Instrumentation for the material analysis of this work consisted of a digital camera, a two-color pyrometer, a broadband radiometer, and three spectrometers as detailed below. During this investigation, the main data of interest comprised the surface response to the incoming air plasma in terms of temperature, mass loss, and species ejected into the boundary layer.

2.1. Plasmatron Facility Description

The VKI Plasmatron facility has been used for the reproduction of the aerothermodynamic environment of atmospheric entry plasma flows, creating a high-enthalpy, highly dissociated subsonic gas flow (Bottin et al. 1999). It is equipped with a 160 mm diameter ICP torch powered by a high-frequency, high-power, high-voltage (400 kHz, 1.2 MW, 2 kV) generator (MOS technology). The gas is heated by induction through a coil, creating a high-purity plasma flow. Three probe holders are installed in the Plasmatron facility next to each other, which can be exchanged independently by a pneumatic mechanism. One holds the test sample, while the other two are used for heat flux and Pitot pressure measurements in the same experimental run as the ablation test. The cold-wall (~350 K) stagnation point heat flux $\dot{q}_{cw}$ is measured with a water-cooled calorimeter having a sensing surface 14 mm in diameter and made of copper. A water-cooled Pitot probe, connected to a Validyne variable reluctance pressure transducer, is used to determine the dynamic pressure of the plasma flow. Atmospheric air at a mass flow of $\dot{m} = 16$ g s^{-1} is used to create the plasma flow. For the results presented throughout this paper, the time indication $t = 0$ s corresponds to the injection of the test sample into the plasma flow. The sample is attached to a sample holder located 445 mm downstream of the plasma jet exit. After reaching the target testing condition (testing chamber static pressure and heat flux), the sample is inserted using the pneumatic mechanism.

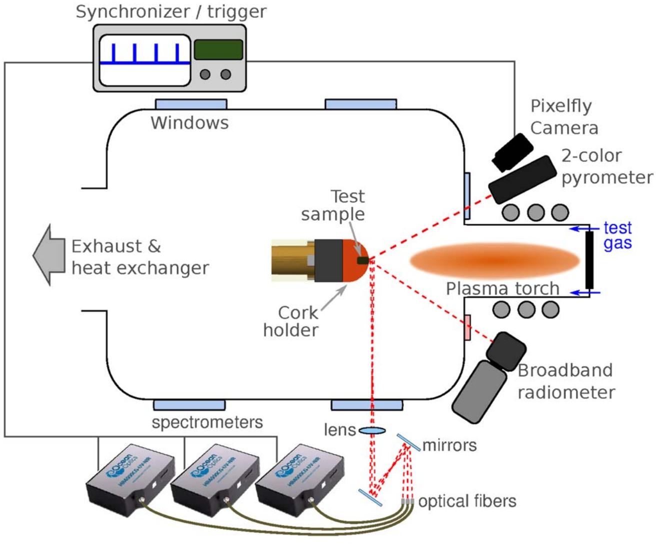

Figure 1. Schematic of experimental setup (not to scale) with diagnostics for meteor ablation analysis.

2.2. Experimental Diagnostics and Methods

A schematic of the experimental setup for in situ ablation measurements can be found in Figure 1 (Helber et al. 2014, 2016a), and is reviewed below. We used a two-color Raytek Marathon MR1S-C pyrometer, employing a wide (0.75–1.1 μm) and narrow (0.95–1.1 μm) spectral band for the temperature determination at a 1 Hz acquisition rate (1300–3300 K). Using two narrow wavelength bands and assuming a constant emissivity over this wavelength range allows an emissivity-independent surface temperature determination. The pyrometer was pointed and focused at the stagnation area of the sample through a 1 cm thick glass window, at an angle of ~35° with respect to the stagnation line. The instrument was calibrated up to 3300 K at the National Physical Laboratory (London, UK) using a high-temperature graphite blackbody, including a spot-size and uncertainty analysis, which resulted in $\delta T_{\mathrm{w}} = \pm 15$ K in the observed temperature range. The highest uncertainty was attributed to the positioning of the pyrometer with respect to the quartz window, introducing measurement inaccuracies.

A broadband infrared radiometer (KT19 HEITRONICS Infrarot Messtechnik GmbH, Wiesbaden, Germany) recorded the surface radiance in a broad spectral range (0.6–39 μm). Assuming a test object following graybody behavior, this instrument allows estimation of the hot wall emissivity using the two-color pyrometer surface temperature as a blackbody radiance reference and the in-band (0.6–39 μm) radiance provided by the radiometer.

For this work, the broadband radiometer was calibrated using a blackbody source up to 1770 K, assuming that emissivity is constant up to 10 μm. The integrated spectral radiance beyond 10 μm ($L_{10\text{–}39\mu\mathrm{m}}$) at this temperature only constitutes 2% of the total radiation and it is thus assumed that emission above 10 μm can be neglected. A KRS-5 window was used for the radiometer measurements as it offers transmissivity over the radiometer operating range.

The front surface was monitored by a 14 bit CCD camera (pco.pixelfly developed by PCO AG) providing snapshots throughout the experiment. Camera acquisitions were triggered using a digital delay generator before injection of the test sample. This allowed for a precise determination of the total injection time. Synchronized with the camera were optical emission spectroscopy (OES) measurements, which consisted of three low-resolution, wide-range Ocean Optics HR4000 spectrometers, providing information on the emission spectrum upstream of the test specimen. The HR4000 spectrometers covered a wide spectral range (200–1000 nm) within a single acquisition and a minimum integration time of 5 ms. The light emitted by the plasma was collected through a variable aperture and focused by a plano-convex, uncoated fused silica lens (LA4745, 750 mm focal length) via two mirrors onto the three optical fiber entries (Ocean Optics QP600-2-SR/BX, $600 \pm 10\,\mu$m core diameter). The optical path was aligned perpendicular to the flow and tangential to the test sample surface. The magnification of the optical system was set to $m = 3$, resulting in a distance between each probing volume of $\Delta d = 2$ mm. The fixed entrance slit width of 5 μm and a 300 grooves/mm grating led to a typical resolution of approximately 0.7 nm full width at half maximum, as was determined using a low-pressure mercury lamp (Oriel 6060), which provides a lower line broadening than covered by a single pixel of the CCD array ($\Delta\lambda_{\mathrm{range}}/3648 \approx 0.22$ nm). For conversion of the data into spectral intensities (W m^{-2} sr^{-1} nm^{-1}), we performed a calibration of the whole system, consisting of the light collection mechanism and the spectrometer efficiency, by placing a tungsten ribbon lamp (OSRAM WI 17G) in the focus of the collection optics inside the test chamber. The lamp was operated at a single power input, producing a stable radiance $I_{\lambda}^{\mathrm{ref}}$, known from prior calibration.

2.3. Test Samples

Two different samples were cut into a cylindrical shape with diameter $d = 16$ mm and length $l = 6$ mm, using a commercial diamond-embedded drill bit. Each sample was embedded in a hemispherical holder of 50 mm diameter and 45 mm length made out of cork-composite ablative material (Figure 2). This sample holder had two main objectives: first, insulating the test sample from side-wall heating, allowing a 1D heat conduction approach and, second, to provide a test shape of known geometry in order to be able to perform an extensive plasma flow characterization by intrusive probes and numerical rebuilding. The employed cork composite material is highly insulating and the only source of heat delivered to the test sample can be assumed to be coming from the stagnation region. A graphite holder of the same geometry was also designed and employed in a second test campaign for which the results are presented in Pittarello et al. (2019). The main disadvantage of the graphite configuration was a strong 3D heating of the test sample due to the high thermal conductivity of graphite, making a numerical analysis of the experimental results difficult. By contrast, the main drawback of using a cork housing was the pollution of the boundary layer with cork ablation products as detected by the spectrometers, as will be seen in Section 4.2. Another possibility for future experiments could be to invest in a water-cooled metallic housing of the meteor sample. This would provide the desired test shape (for example, hemisphere) without polluting the boundary layer, and at the same time would provide 1D thermal conduction inside the sample if well insulated from the cooled holder walls. Unfortunately, such thermal insulation from the side-walls would not be trivial as ablation of the sample was one main objective, which would lead to destruction of the insulation material as well, again polluting the test material and boundary layer. We suggest using a pure test sample, as done by Loehle et al. (2017), without any additional interfaces that could contaminate the recorded data, such as a single sample in the desired test shape (e.g., hemisphere). However, meteorite samples for such destructive tests are difficult to obtain, especially at a reasonable size to be machined into the desired shape, and the strong side-wall heating in such case would make the thermal analysis more difficult compared to the 1D approach we applied in this work. In addition, such a sample might be completely destroyed during the experiment because of the rapid heating, hampering recovery and further analyses of the resulting material (no material remainders were analyzed in Loehle et al. 2017).

Two different materials were chosen as test samples: a fragment of AB serving as an analog meteoritic material, and a piece of El Hammami H5 OC. Their main characteristics are reported in Table 2. The densities were obtained by weighing the samples and assuming a perfectly cylindrical shape. Physico-chemical properties determined by X-ray fluorescence (XRF) and scanning electron microscopy (SEM) are briefly presented below.

Alkali basalt. Being a mineralogically simple material, basalt is one of the most common igneous rocks on Earth and its bulk composition roughly resembles that of chondrites and more closely matches stony achondrites. This specific sample is an AB with approximately 50 wt% of SiO_2. The chemical composition of the basalt was determined by means of μ-XRF and SEM-EDS and the results are presented in Table 3. For details on the analytical conditions, we refer to Pittarello et al. (2019). The semi-quantitative analysis shows a material particularly enriched in volatiles with SiO_2 and Al_2O_3 as major components, indicating a high feldspar content typical of mafic, basaltic rocks. Basalt densities commonly vary between 2700 and 3300 kg m^{-3}, making our sample slightly lighter (2400 kg m^{-3}) than average basalt. The equilibrium melting

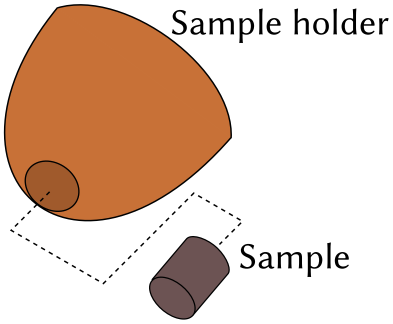

Figure 2. Schematic of the sample and its cork holder. The material sample (ordinary chondrite or alkali basalt), 16 mm in diameter, is embedded in the sample holder in a stagnation point configuration.

Table 2
Characteristics of the Two Samples

Material ID	l (mm)	d (mm)	m (g)	ρ (kg m^{-3})
AB	6	16	2.74	2400
OC	6	16	3.65	3026

Table 3
Major Species Chemical Composition before the Experiments

Species	AB (wt%)	OC (wt%)	OC-Ref. (wt%)
SiO_2	52.28	50.71	36.6
TiO_2	1.23	0.07	0.1
Al_2O_3	22.33	1.74	2.1
Na_2O	6.66	1.55	0.8
K_2O	6.09	0.10	…
CaO	5.16	2.33	1.7
FeO	4.95	15.93	11.9
MgO	0.61	26.03	23.1

Note. Chemical composition was determined by means of μ-XRF for the alkali basalt (AB) and laser ablation–ICP–mass spectrometry for the ordinary chondrite (OC-silicate portion). For the latter, a reference value from literature is also provided (Jarosewich 1990).

temperature of most basalts is generally in the range between 1273 and 1473 K, whereas average thermal conductivities vary between 1.69 and 2.11 W m^{-1} K^{-1} (Eppelbaum et al. 2014). The specific heat of basalts is generally between 840 and 1230 J kg^{-1} K^{-1} with a heat of fusion of ~500 kJ kg^{-1} (Kojitani & Akaogi 1995).

Ordinary chondrite. OCs represent the vast majority of all meteorites recovered on Earth. These meteorites are thought to come from a relatively small number of asteroids located in near-Earth orbits (e.g., Vernazza et al. 2015). They comprise a range of particle types, from fine dust-like matrix to millimeter-scale chondrules, which are solidified molten droplets after which chondrites are named. They are often considered the primary building blocks of most large solar system objects. Among these, class H OCs have a relatively reduced chemical composition and therefore are suitable to highlight possible redox processes induced by interaction with atmospheric oxygen. The class H OC El Hammami (petrologic type 5) was selected. The petrologic type defines the thermal metamorphism experienced in the parent body, from 3 to 6 (or 7) for OCs, for increasing chemical equilibration. A meteorite with a high petrologic type (5–6) will therefore exhibit homogeneous compositions for each mineral phase. The chemical characterization of a silicate portion of the sample obtained via laser ablation–ICP–mass spectrometry (Pittarello et al. 2019) is reported in Table 3, where the average composition of H chondrites reported by Jarosewich (1990) is also presented as a reference. In Yomogida & Matsui (1983), the authors computed bulk densities in a range between 3350 and 3690 kg m^{-3} for H chondrites. In the same study, thermal conductivities were measured between 0.415 and 3.85 W m^{-1} K^{-1}. In the case of H chondrites, the specific heat range is 500–900 J kg^{-1} K^{-1} between 200 and 600 K (Yomogida & Matsui 1983), while several studies show average values around 700 J kg^{-1} K^{-1} for temperatures close to 300 K (Consolmagno et al. 2013).

3. Test Parameters and Rebuilding of Flight Free-stream Conditions

The local heat transfer simulation methodology was originally developed by Kolesnikov (1993), allowing us to duplicate flight conditions at the stagnation point by matching the boundary layer edge total enthalpy h_e, pressure p_e, and the radial velocity gradient in the radial direction at the wall ($\beta_e = (\partial u/\partial x)_e$) between ground experimental and flight conditions.

The subsonic Plasmatron flowfield was numerically simulated by solving the Navier–Stokes equations coupled with the Maxwell equations for the electromagnetic field created by the coil (VKI ICP code; Vanden Abeele & Degrez 2000; Degrez et al. 2004; Magin & Degrez 2004). This provides the boundary layer velocity gradient β and boundary layer thickness δ, as well as an initial streamwise velocity v for the characterization of the boundary layer around the test sample under local thermodynamic equilibrium and axisymmetric flow assumptions (Barbante & Chazot 2006). The hydrodynamic boundary layer edge parameters (temperature T_e, density ρ_e, and velocity v_e) are determined through an iterative procedure using the VKI boundary layer code (Barbante et al. 2002), which takes as input conditions the flow quantities determined from the VKI ICP code, as well as the experimental heat flux and Pitot pressure measurements. The VKI boundary layer code consists of solving the chemically reacting stagnation line boundary layer over a catalytic surface under chemical nonequilibrium conditions, assuming fixed wall catalytic properties for copper and a cold-wall temperature for the heat flux probe. A more detailed description of this procedure applied to ablation tests can be found in Helber et al. (2015).

We chose three test conditions, often used for TPS testing, which are characterized by a high level of confidence in terms of repeatability and flow behavior. In addition, these experimental conditions were chosen to allow the recovery of the sample for surface characterization analysis after the tests. The experimental conditions are listed in Table 4. In this work, we present results for condition (1), while conditions (2) and (3) are relevant for the surface characterization presented in Pittarello et al. (2019). Notice that the cold-wall heat flux $\dot{q}_{cw}$ was measured by means of a cylindrical calorimeter probe for condition (1) and a hemispherical calorimeter probe for conditions (2) and (3). The values presented in Table 4 are given for a hemispherical calorimeter, or its equivalent for condition (1).

Table 4
Plasmatron Test Conditions

Condition ID	Experimental p_s (hPa)	P_{el} (kW)	$\dot{q}_{cw}$ (MW m^{-2})	Numerical h_e (MJ kg^{-1})	ρ_e (g m^{-3})	T_e (K)	v_e (m s^{-1})	β (1 s^{-1})
(1)	200	206	1.2	24	7.0	6293	26	1230
(2)	220	310	3.0	42	4.3	8079	55	4480
(3)	15	373	3.1	54	0.3	9229	687	29790

Note. Data include experimentally measured static pressure p_s, generator electric power P_{el}, and mean cold-wall heat flux $\dot{q}_{cw}$, as well as numerically rebuilt boundary layer edge values of enthalpy h_e, gas density ρ_e, gas temperature T_e, velocity v_e, and boundary layer gradient β_e.

A numerical procedure was used to infer flight conditions from the experimental ones. By solving the Rankine–Hugoniot jump relations, assuming a thermally perfect gas, a contour map of post-shock enthalpy h_e and pressure p_e was defined for a range of free-stream velocities and altitudes. An equivalent flight radius can also be computed by means of modified Newtonian theory (Anderson 1989):

$$R_{equ,f} = \frac{1}{\beta}\sqrt{\frac{2(p_e - p_\infty)}{\rho_{e,f}}} \tag{1}$$

where p_∞ represents the atmospheric pressure at the flight altitude and $\rho_{e,f}$ the flight boundary layer edge density obtained from the Rankine–Hugoniot jump relations. The three experimental conditions are shown in Figure 3. For the experimental results reported here, condition (1) corresponds to a 3.8 m diameter object ($2 \times R_{equ,f}$), flying at a velocity of 6.9 km s^{-1}, at an altitude of 54.7 km. Fireball trajectories for two well-known events are also reported in Figure 3: one can observe that the range of velocities of the two bolides, Benešov and Chelyabinsk, are higher than our experimental conditions. We chose a lower heat flux condition than what can be assumed from existing meteor observations to avoid complete destruction of the samples and ensure successful recovery of the modified basaltic and chondritic materials. Recovery of modified experimental samples enabled us to set a further objective in this experimental campaign, which was a complete petrographic and geochemical characterization and comparison with natural meteorite fusion crust. Future work may include testing at higher heat fluxes, reproducing smaller meteoroids at higher entry velocities.

It should be noted here that most of the mass of extraterrestrial material falling on Earth consists of micrometeorites (between 50 and 2000 μm, producing 40,000 ± 20,000 metric tons of extraterrestrial matter to Earth every year; Love & Brownlee 1993). But most significant discoveries about meteorite parent bodies and the early stages of the solar system formation have so far been made by focusing on actual meteorites. It is therefore important to constrain the modifications induced on this material during atmospheric entry. Micrometeorites, including their innermost parts, undergo degassing, melting, and evaporation, with limited material remaining as required for high-precision analytical studies. To amplify the detectable effects of atmospheric passage on geological materials and at the same time recover material required to make our observations, we opted for the experimental design described above.

Table 5
Overview of Plasmatron Results for Condition (1)

Material	τ (s)	T_w (K)	Δm (mg)	ϵ ($\cdots$)
AB	8	2280	n/a	0.74
OC	21	2360	3	0.69

Note. Data for alkali basalt (AB) and ordinary chondrite (OC) include test sample exposure time τ, mean surface temperature T_w, total mass loss Δm, and surface emissivity ϵ. Due to the fracturing of the material, the total mass lost by the basalt sample could not be determined.

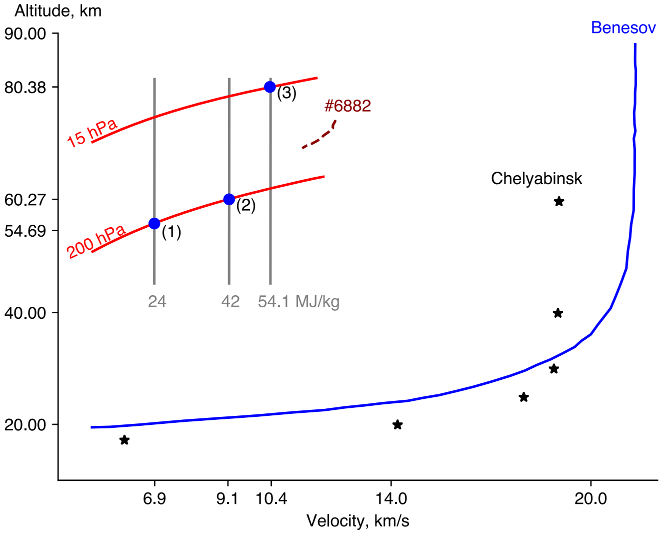

Figure 3. Duplication of the Plasmatron test conditions to flight conditions. The Benešov fireball reported by Borovička & Spurný (1996) has an estimated value at entry conditions of 2.3 m diameter body with 21.3 km s^{-1} velocity. The Chelyabinsk event (Borovička et al. 2013) is estimated to be 18 m in size, with an entry velocity of 19 km s^{-1}. The trajectory #6882 is one of the 413 photographic meteors reported by Shepard et al. (1967) and Jacchia & Whipple (1961). The sizes of these bodies are not reported.

4. Experimental Results

In Table 5, we present an overview of the main results for both materials in terms of maximum surface temperature, test time, and total mass loss. In our tests, the basalt sample broke soon after injection into the plasma (after ~8 s) and the test run was aborted. In a similar experiment, not further detailed in this paper, the sample was first dried at 120 °C for two hours to remove any possible water contamination and was also held in a cork holder with a gap between the lateral side of the sample to release any mechanical stress on the basalt sample from an expansion of the cork. However, also in this experiment the

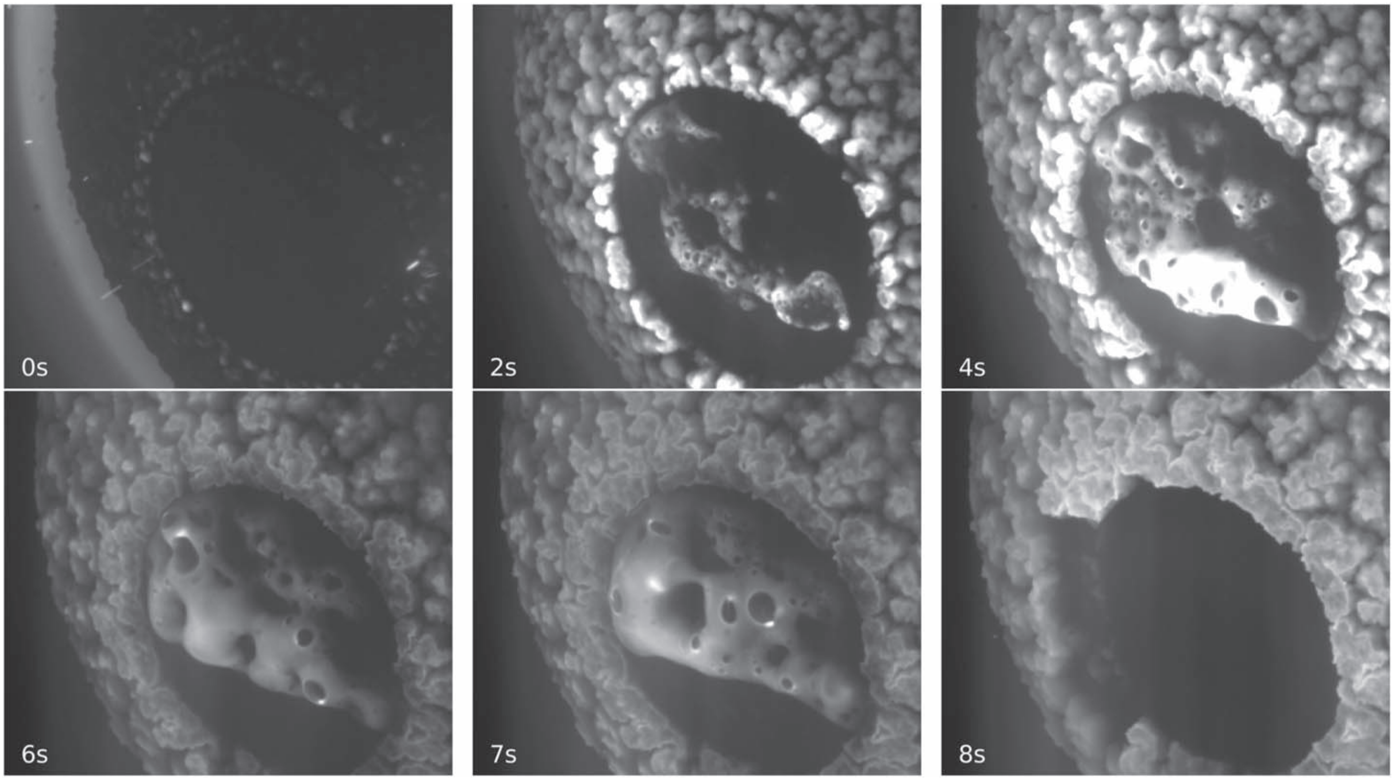

Figure 4. Snapshots (upper left to lower right) during the AB test at 1.2 MW m^{-2} and 200 hPa highlighting boiling of the surface after 2 s (time from injection indicated in each image); the sample broke out of the sample holder after 8 s and the test was aborted.

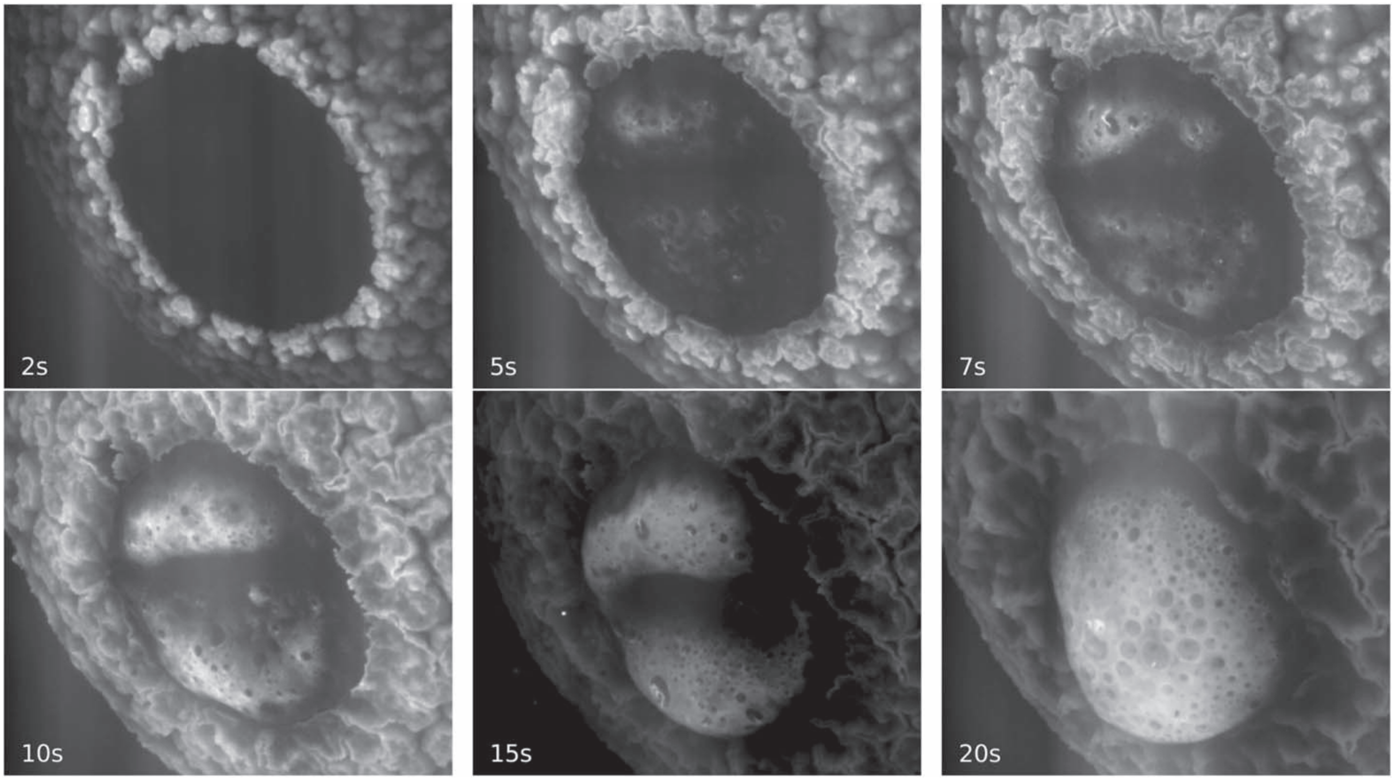

Figure 5. Snapshots (upper left to lower right) during the OC test at 1.2 MW m^{-2} and 200 hPa highlighting boiling of the surface after 5 s (time from injection indicated in each image); a melted surface state remained present throughout the remaining 15 s of the test.

basalt underwent fracturing, which can be ascribed to thermal fracturing, probably resulting from the mineral flow fabric (crystal alignment reflecting flow of the original lava before solidification) and strong, igneous crystalline texture. Anisotropies in the basalt result in internal stress during temperature increase, due to different thermal expansion coefficients among

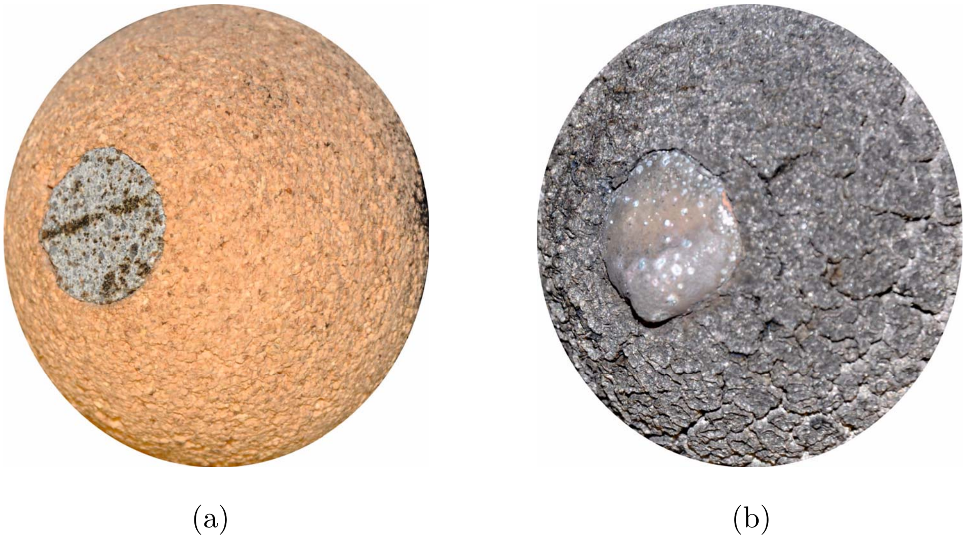
(a) (b)

Figure 6. OC samples before (a) and after (b) plasma exposure.


(a) (b)

Figure 7. AB (a) and OC (b) samples after plasma exposure. In (a), glassy features formed after the resolidification. In (b), a change of color, probably a sign of the change in the oxidation state of iron, is visible.

minerals or even preferred orientation of minerals. In contrast, the OC withstood the plasma flow during the entire test time of 21 s without fracturing, probably because of a predominantly granular metamorphic texture (rather than igneous). In fact, the OC sample only lost 3 mg during those 21 s, starting from an original weight of 3.65 g. This illustrates that, although the surface appeared to be boiling and frothing, only a little material volatilization took place and not much mass was injected into the boundary layer, allowing recovery of the ablated material.

Snapshots taken throughout the experiment indicate the formation of gas bubbles on the surface, shown in Figures 4 and 5. The frothing appeared earlier for the AB sample (after 2 s of plasma exposure) than for the OC (5 s after plasma exposure). A possible explanation for this observation may lie in the fast evaporation of the volatile elements for which the concentration is considerably higher in the basalt sample (see Table 3). In gases of solar composition, Na and K have 50% condensation temperatures of 958 K and 1006 K respectively; for Fe this is 1334 K (Lodders 2003). One should note that during hypersonic flight this frothing layer can be removed by the aerodynamic forces as suggested by Allen & Baldwin (1967).

Photographs taken before and after each experiment are shown in Figures 6 and 7. The AB had glassy features on its surface after resolidification upon cooling. These glasses have roughly the same composition as the basalt, with apparent depletion in highly volatile elements (Na and K). The OC, however, displayed a reddish color change, which probably indicates a change of the oxidation state of the high iron content with formation of hematite (Fe_2O_3) at the surface. Global oxidation of the sample is also suggested based on petrographic observations of the resulting material, which contains magnetite (Pittarello et al. 2019).

4.1. Surface Temperature Measurements

The plateau temperatures reached during these test conditions were 2280 K for the AB (Figure 8(a)) and 2360 K for the OC (Figure 8(b)). Although the pyrometers measuring surface areas of 11 mm diameter mostly covered the basalt and chondrite sample surfaces, some additional radiation, coming from the cork housing, may have been recorded by the pyrometer. This cork housing is likely to have resulted in a different surface temperature from the held samples, as well as in different apparent emissivities, affecting the measured temperatures to a small degree.

The delayed temperature rise of the pyrometer with respect to the radiometer in Figure 8 originated from a higher low-temperature limit for the pyrometer. In particular, for the intact OC sample, the cooling curve due to surface radiation and internal conduction after the plasma was turned off can be clearly

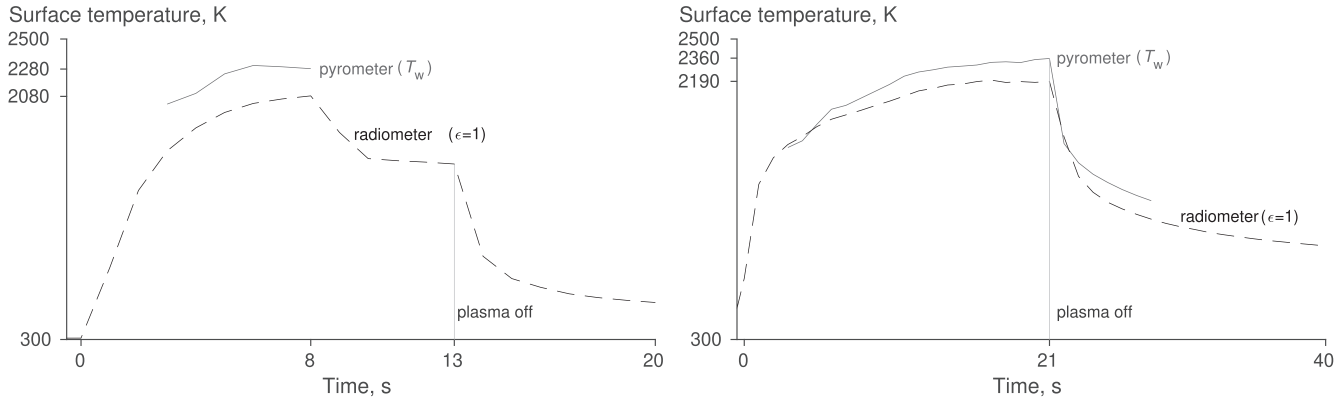

(a) (b)

Figure 8. Surface temperature evolution (T_w, full lines) of AB (a) and OC (b); radiometer measurements (dashed lines) were recorded in a wider temperature range but for $\varepsilon = 1$ (see the text); Once the plasma is switched off (AB: 13 s, OC: 21 s), the surface temperature drops immediately due to the high thermal radiation.

observed. In addition, the broadband radiometer measurement served to provide an average apparent directional emissivity at those temperatures for both materials ($T^4_{\varepsilon=1,0.6-39\,\mu\mathrm{m}}/T^4_\mathrm{w}$). This resulted in an emissivity of $\varepsilon_{0.6-39\,\mu\mathrm{m}} = 0.69$ for the AB sample and in $\varepsilon_{0.6-39\,\mu\mathrm{m}} = 0.74$ for the OC. Those data will be used below in Section 5 for comparison with a 1D numerical model.

4.2. Optical Emission Spectroscopy

We present emission spectra recorded in front of the test sample during plasma exposure in Figure 9. The three plots present the radiative signature of the air plasma free-stream (red) together with radiation mostly coming from the ablating cork holder just at injection (a), an emission spectrum recorded in front of the AB sample shortly after injection (b), as well as one recorded in front of the OC sample several seconds into the test (c), when radiative emission was highest. The free-stream emission spectrum presents expected CN violet and N_2^+ radiation, both strong radiators and generally present in atmospheric air plasmas at such gas temperatures (5000–10,000 K). The ablating cork sample, in addition, led to much stronger CN violet emission due to ablation, as well as sodium and potassium. Traces of the volatile elements sodium and potassium in this spectrum may also result from the ablation of the test sample. However, sodium has also been found in the cork material as a result of either the supplier's manufacturing process, or in-house machining of the sample holder.

Table 3 indicates that both materials contain sodium and potassium, and the latter is especially true for basalt. A small contribution of the C_2 Swan system can also be identified between 440 and 550 nm, also due to the ablating cork cover, which is well known to result from the pyrolyzation of typical charring thermal protection materials (Helber et al. 2014, 2016b).

The spectral intensity signal observed by the spectrometers strongly changed during the ablation of the AB or OC. Both spectra are mainly dominated by iron emission, with several strong lines in the UV and visible range of the spectrum, as indicated by the fine markers. As seen in Table 3, high concentrations of iron are present in both samples. Again, the volatile elements sodium and potassium are strongly present; their temporal and spatial emission profiles will be discussed below. The recorded emission signals of sodium (589 nm) actually saturated during the measurement, and therefore did not allow further analysis of their temporal emission profiles. The saturation is not apparent from the plots of Figure 9 as emission lines at lower and higher wavelengths are well captured (at higher calibrated intensity); this comes from the lower quantum efficiency of the HR4000 sensor toward its wavelength wings below 400 nm and above 750 nm.

In addition, especially in the case of AB, strong silicon emission was also visible at 252 and 288 nm. Interestingly, although both sample materials are predominantly composed of SiO_2, the OC did not show any silicon emission during the whole experiment. In general, moderately refractory elements like silicon, magnesium, and truly refractory elements such as aluminum, which are part of the OC elemental composition, are not strongly present in the spectrum. (In solar gases and with a 50% condensation temperature of 1653 K, aluminum is considered truly refractory (1500–1700 K); silicon (1310 K), magnesium (1336 K), and iron (1334 K) are considered moderately refractory (1300–1500 K; Lodders 2003.) The emission of iron lines produced by an ablating OC sample in plasma flows was also reported by Loehle et al. (2017), together with traces of silicon, sodium, potassium, and manganese.

In addition to the radiative species emission, continuum radiation, emitted by the hot surface, was recorded by the spectrometer closest to the surface (Figure 9). This might have been caused by the cork material which tends to swell upon heating, with emission of the hot surface reaching the optics of the closest spectrometer.

Potassium and sodium emission during ablation of meteoritic samples are of particular importance and high interest to the community. However, several constraints limited the possibility of obtaining unpolluted emission spectra from the observed material alone. One limiting factor was the available test sample dimension, which was a cylinder of 16 mm diameter, so an adequate sample holder needed to be used. We decided to embed the test sample in a holder of known shape (i.e., a hemisphere) in order to be able to perform an extensive plasma flow characterization by intrusive probes and numerical rebuilding.

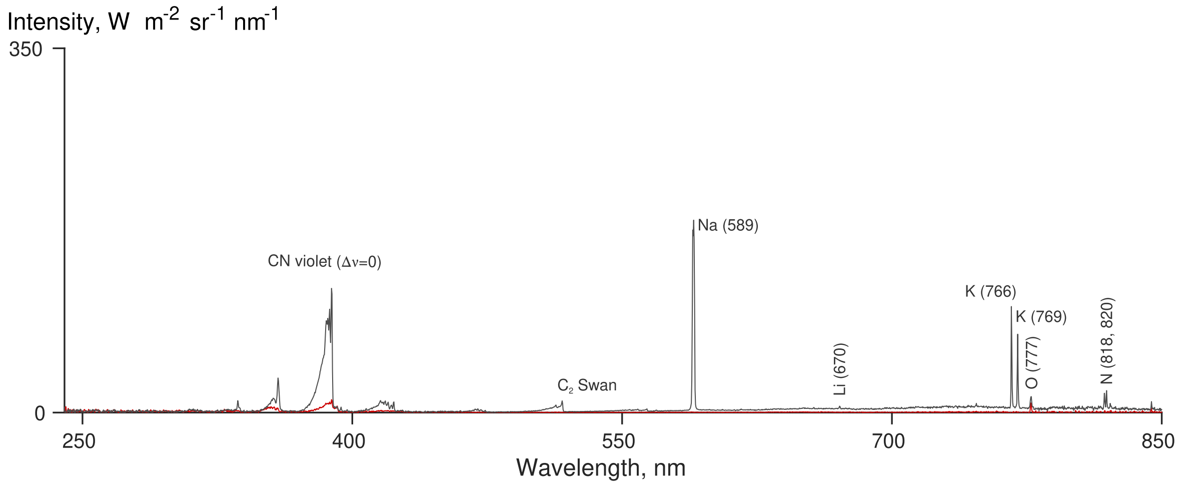

(a) Air plasma free-stream (red) and cork holder (gray) at injection

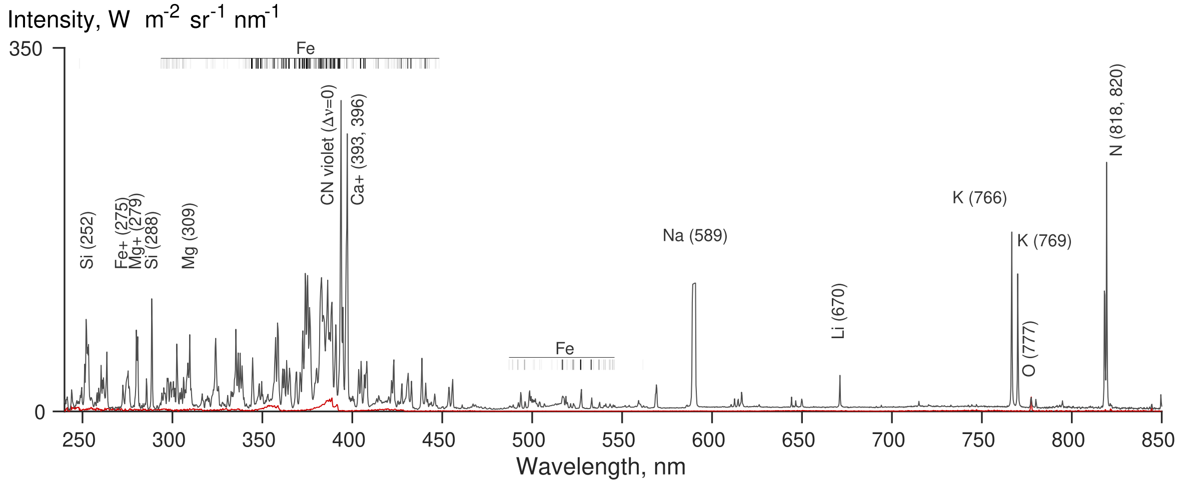

(b) Alkali basalt at injection (gray) and air plasma free-stream (red)

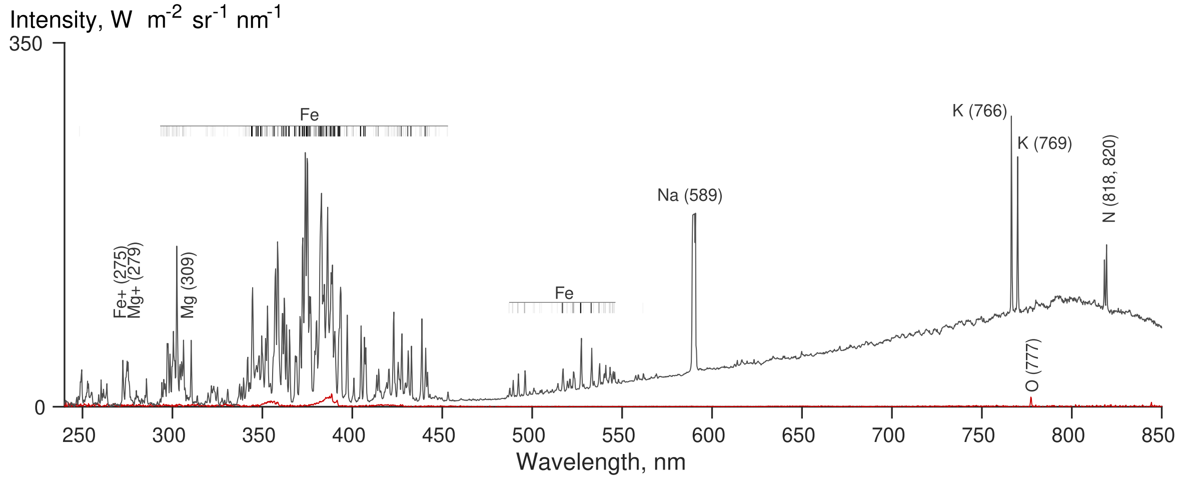

(c) Ordinary chondrite after 16 s (gray) and air plasma free-stream (red)

Figure 9. Emission spectra overview of air plasma and cork holder (a), AB (b), and OC (c) tests; the air free-stream spectrum for each test run is given in red, while the spectrum recorded in front of the ablating material sample is given in gray, highlighting the presence of additional radiative contributors ejected by the material (all spectra recorded by the spectrometer closest to the surface).

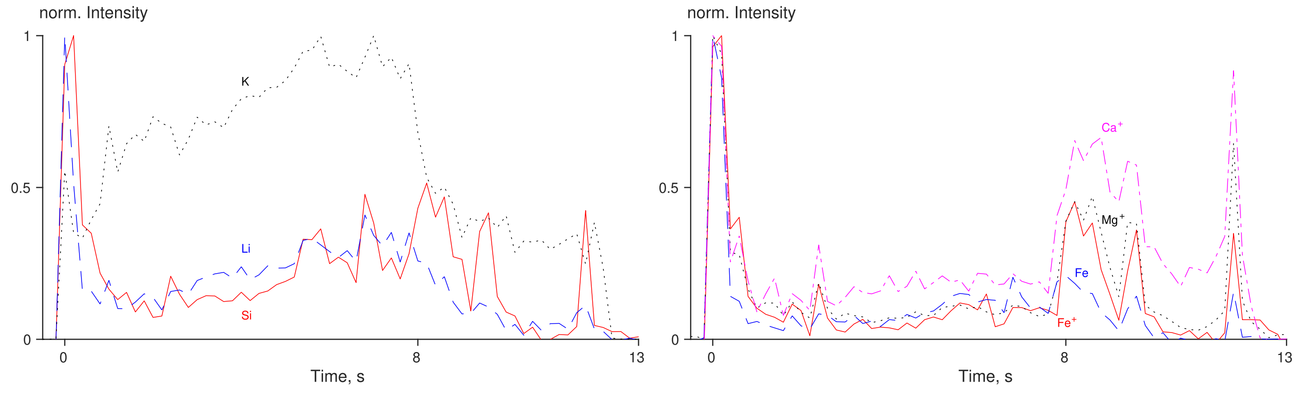

(a) (b)

Figure 10. (a) Temporal emission profiles of Si (full), K (dotted), and Li (dashed) as well as (b) of Ca^+ (dashed–dotted), Mg^+ (dotted), Fe (dashed), and Fe^+ (full) during AB ablation showing a strong emission peak at injection of the test sample; a sudden emission decrease of K and an increased emission for Fe, Mg^+, and Ca^+ were then visible when the sample broke after 8 s (all data recorded by the spectrometer closest to the surface).

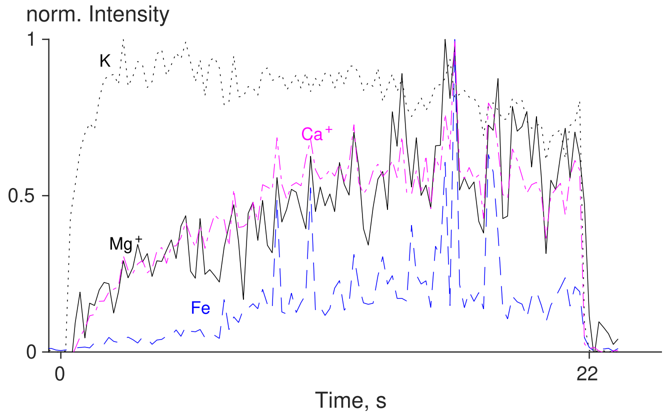

Figure 11. Temporal emission profiles during OC ablation showing a fast rise of the alkali metal K (dotted), followed by a rise of the alkaline earth metals Ca^+ (dashed–dotted), Mg^+ (full), and finally Fe (dashed) (all data recorded by the spectrometer closest to the surface).

4.2.1. Temporal Emission Profiles

From the temporally resolved emission spectrum data, we obtained the normalized temporal emission profiles of the main radiating species, presented for AB in Figure 10 and for OC in Figure 11. The main behavior of each emission profile is different for each material: the temporal emission of all species resulting from AB presented a strong peak at injection into the plasma flow, followed by a strong emission drop. This was not the case for the OC sample, where an emission rise was observed toward the end of the test. The temporal emission rose immediately for the alkali metal potassium, followed by a rise of the alkaline earth metals Ca^+ and Mg^+, with finally a slow rise of iron.

In both cases, potassium emission is persistent from the beginning of the test. The potassium doublet at 766 nm was observed by Loehle et al. (2017) and Agrawal et al. (2018) in their ground experiments of the OC. Moreover, Borovička et al. (2008) successfully detected the same potassium doublet in meteor spectra observations, suggesting that emission at this wavelength might be usually absorbed by atmospheric oxygen, a possible reason why it is typically not detected. From the snapshots we observed an almost immediately boiling AB surface (Figure 4), whereas the OC heated up more slowly, reaching a steady boiling phase (Figure 5). The same behavior can be observed in the temporal emission profiles. This is especially visible in Figure 11 for the iron emission.

Figure 10 further shows the effect of the mechanical fracturing of the basaltic sample at 8 s into the test as was already observed from Figure 4. First, the fracturing of the sample causes an abrupt drop in the emission profile of potassium, Figure 10(a). This strengthens the likelihood that a large part of potassium emission comes directly from the sample. Since sodium emission was saturated for all three spectrometers over time for both test cases, no temporal emission profiles are presented. Second, the emission spectrum of several species originating from basalt such as Fe^+, Mg^+, and Fe responded with a short rise in intensity at around 8 s, as seen in Figure 10(b). The same fluctuation trends were observed for silicon at around 8 s in Figure 10(a).

4.2.2. Temporal Emission at Three Locations in the Boundary Layer

Three spectrometers were focused in the boundary layer in front of the test sample (Figure 1), with a distance of 2 mm between each other. The temporal emission profiles of silicon and potassium recorded at the three locations in the boundary layer (close to the surface, then increasing by 2 mm increments away from the surface) are displayed in Figure 12. Those profiles are presented in absolute units and have been obtained by integrating the calibrated line-of-sight spectral signal over a wavelength range (enclosing the line wings) for each transition of each individual spectrum. Background emission originating from the sample surface or other radiating contributors was removed by fitting a baseline on the line shape edges and subtracting all underlying radiation.

While silicon showed an emission peak at injection, probably caused by strong pyrolysis outgassing (blowing) within the first second as the cork material heats up, potassium slowly rose during the experiment until the sample broke after 8 s. Interestingly, the potassium emission does not follow the same trend at the three locations in the boundary layer. This might be due to changing chemistry at the basalt surface or inside the boundary layer, as well as due to the higher gas temperatures at greater distances from the surface.

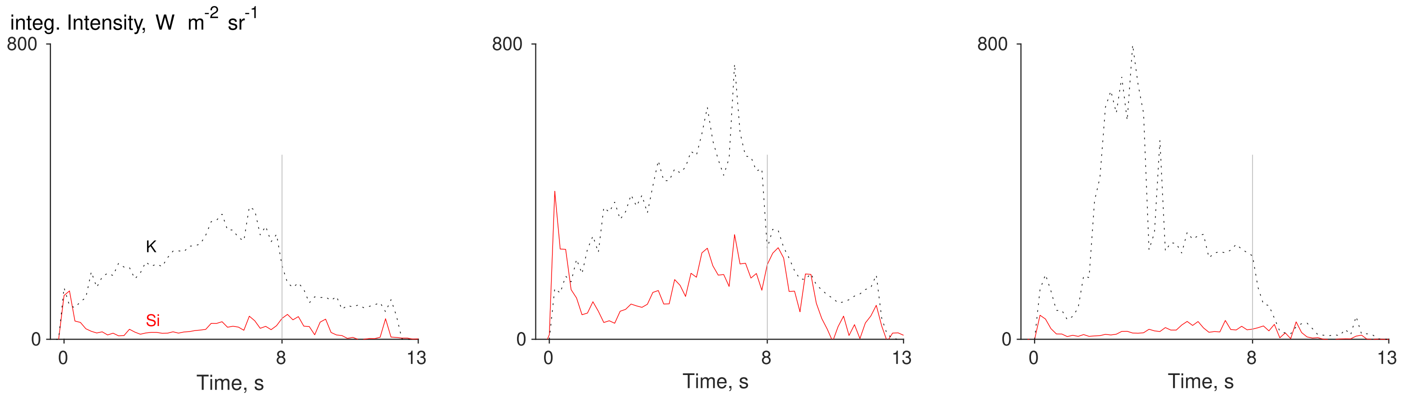

Figure 12. Emission profiles of potassium (dotted) and silicon (full) recorded by the three spectrometers during AB ablation (left: close to surface; middle: away from surface; right: far from surface, in 2 mm increments). An emission peak of silicon at test start was observed for silicon; potassium, however, rose during sample injection at all three locations until dropping after 8 s when the sample broke.

4.3. Chemical and Petrographic Characterization of the Resulting Material

Regarding the AB, the resulting material after the experiment mostly consisted of homogeneous glass. The chemical composition of the glass, in comparison with that of the basalt before the experiment, showed apparent enrichment of the melt in titanium, iron, and manganese and depletion in sodium and potassium. The depletion of highly volatile alkali metals (sodium and potassium) supports the OES measurements during the experiment. On the surface of the glass, spherical objects were observed, with an average composition rich in SiO_2, Na_2O, and K_2O, suggesting condensation from the vaporized material.

The melting of the OC, despite quite rapid quenching, resulted in extensive crystallization after the experiment. A rough comparison between the bulk composition of the resulting material and the interior of the sample, unaffected by melting, showed that the melt was overall enriched in TiO, FeO, and Cr_2O_3. This apparent enrichment might result from the depletion in most volatile or moderately volatile elements. The crystallized phases were olivine and magnetite, suggesting oxidation of the iron originally in the metal state. Detailed characterization of the resulting material from both experiments is provided in Pittarello et al. (2019).

5. Modeling of the Material Response of the H5 Chondrite

The thermal response of the material was studied and compared with the experimental data by solving numerically the heat conduction equation $\partial T/\partial t = k/(\rho c_p)\ \partial^2 T/\partial x^2$ in a 1D Cartesian domain. The choice of the 1D approximation is supported by the good insulation properties of the cork holder. At the stagnation point, we applied a boundary condition built as a surface energy balance between the gas and the liquid phase:

$$\dot{q}_{\mathrm{w}}^{\mathrm{conv}} + \dot{q}_{\mathrm{w}}^{\mathrm{chem}} = k\frac{\partial T}{\partial x}|_{\mathrm{w}} + \epsilon\sigma(T_{\mathrm{w}}^4 - T_\infty^4) + \dot{m}_v L_v. \tag{2}$$

The left-hand side represents the heat due to the impinging plasma flow $\dot{q}_{\mathrm{w}}^{\mathrm{conv}}$ and heterogeneous chemical reactions $\dot{q}_{\mathrm{w}}^{\mathrm{chem}}$, while the right-hand side comprises the energy loss due to the thermal conduction inside the material, re-radiation, and net evaporation of the surface. Concerning the physical properties, density ρ and emissivity ϵ were measured. The specific heat c_p and latent heat of vaporization L_v were constrained to the values chosen by Vondrak et al. (2008) and Campbell-Brown et al. (2013) and are summarized in Table 6.

Table 6
Physical Properties Assumed for Numerical Modeling of the Thermal Response in the Samples

Material ID	ρ (kg m^{-3})	k (W m^{-1} K^{-1})	ϵ ($\cdots$)	c_p (J kg^{-1} K^{-1})	L_v (J kg^{-1})
AB	2400	0.7	0.69	800	6×10^6
OC	3026	3	0.74	1000	6×10^6

Note. Densities were measured by weighing the cylinders and emissivity calculated as described in Section 4.

The convective contribution can be estimated by the Fay & Riddell (1958) formula:

$$\dot{q}_{\mathrm{w}}^{\mathrm{conv}} = \frac{\mathrm{Nu}}{\sqrt{\mathrm{Re}}}\sqrt{\rho_{\mathrm{w}}\mu_{\mathrm{w}}\beta}\left(\frac{h_{\mathrm{e}} - h_{\mathrm{w}}}{\mathrm{Pr}}\right), \tag{3}$$

where the non-dimensional parameters are the Nusselt (Nu), Reynolds (Re), and Prandtl (Pr) numbers. The Reynolds number is computed based on the equivalent radius. The subscript "w" is used to refer to the stagnation point condition at the wall, while "e" represents the edge of the boundary layer. More information about this approach can be found in Turchi et al. (2015). Condition (1) reported in Table 4 corresponds to a cold-wall convective heat flux of 1.2 MW m^{-2}.

In Section 4.3, the change in composition of the OC was interpreted as a possible change in the oxidation state of iron species, resulting in crystallization from the melt of magnetite (Fe_3O_4) and of olivine richer in FeO than the original olivine. The formation of magnetite can be described using a hematite-like component (Fe_2O_3), which is diluted by FeO in the sample. Since oxidation is a strongly exothermic process, one cannot exclude the possibility of such reactions contributing to the energy balance by releasing their formation enthalpy at the wall. Genge (2016) showed, that oxidation is important for iron micrometeoroids because it proceeds faster than vaporization. The author reports that for wüstite (FeO)-dominated particles an increase in mass of up to 23% by reaction with atmospheric oxygen can occur. In this work, we consider reactions of the following type, $2\mathrm{FeO}_{(l)} + \frac{1}{2}\mathrm{O}_{2(g)} \rightarrow \mathrm{Fe_2O}_{3(l)}$ and $\mathrm{Fe}_{(l)} + \frac{1}{2}\mathrm{O}_{2(g)} \rightarrow \mathrm{FeO}_{(l)}$.

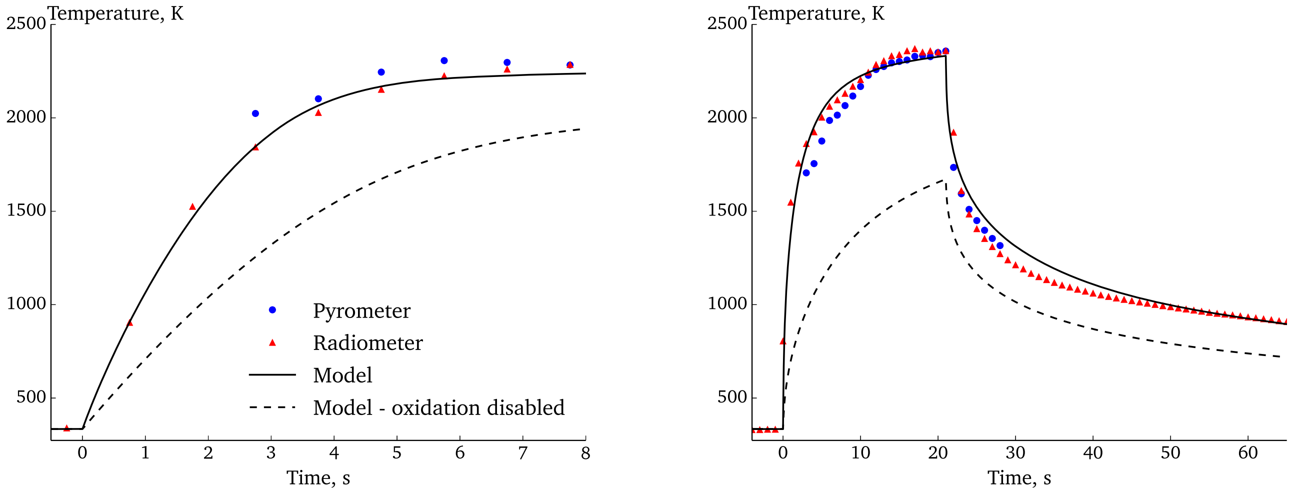

(a)

(b)

Figure 13. Comparison of the surface temperature measurements (blue bullets: pyrometer, red triangles: radiometer with estimated emissivity) with the numerical simulation of the thermal response of the AB (a) and OC (b). Exothermic heterogeneous reactions play an important role as discussed in Section 4.3 and have a significant impact on the simulations (full lines: model including oxidation reaction, dashed lines: oxidation disabled). We used the same parameter γ_r for modeling the basalt response as chosen for the ordinary chondrite.

The chemical heat flux related to the former reaction can be written as:

$$\dot{q}_{\rm w}^{\rm chem} = 2\gamma_r\, p_{{\rm O}_2}\sqrt{\frac{m_{{\rm O}_2}}{2\pi k_B T_{\rm w}}}\,\Delta H^0_{{\rm Fe}_2{\rm O}_3}\, x_{\rm FeO}, \qquad (4)$$

which is obtained by multiplying the impinging oxygen flux for the enthalpy of reaction, $\Delta H^0_{{\rm Fe}_2{\rm O}_3}$, rescaled by the molar concentration $x_{\rm FeO}$ of FeO in the material. This was computed under the assumption of local thermodynamic equilibrium using the Plasmatron chamber pressure (which for this condition practically equals total pressure inside the flowfield) and test sample wall temperature $T_{\rm w}$. In this formula, γ_r plays the role of a recombination probability for the impinging molecular oxygen at the surface and the factor 2 provides the correct stoichiometric constraint.

Now, we estimate the relative importance of the oxidation term with respect to the evaporation one in Equation (2). Since $\Delta H^0_{{\rm Fe}_2{\rm O}_3} \approx L_v$, then $\dot{q}_{\rm w}^{\rm chem} = 2\dot{m}_{\rm ox} L_v$ and their net contribution to the global surface energy balance, $\dot{q}_{\rm w}^{\rm chem} - \dot{m}_v L_v$, can be written as follows:

$$2\dot{m}_{\rm ox} L_v - \dot{m}_v L_v = \frac{1}{2}\dot{q}_{\rm w}^{\rm chem} + (\dot{m}_{\rm ox} - \dot{m}_v) L_v \approx \frac{1}{2}\dot{q}_{\rm w}^{\rm chem}, \qquad (5)$$

where $\dot{m}_{\rm ox}$ is the input of the oxidation reactions to the overall mass balance. The term containing L_v is negligible when compared to the first one, as it is proportional to the small mass loss, $\frac{1}{\pi d^2}\frac{\Delta m}{\tau} L_v$. This result is used as input in Equation (2).

In Figure 13, a comparison between the simulated and experimental values of the wall temperature is shown. Both measurements are presented, the emissivity-independent pyrometer measurement (blue bullets), as well as the emissivity-dependent radiometer measurement (red triangles), accounting for the estimated emissivity (Section 4.1). This was done because the radiometer presents a wider temperature range and was able to capture heating up of the material from room temperature as well as full cooling down.

The heterogeneous exothermic reactions play an essential role in the energy balance and have a significant impact on the temperature profiles, as demonstrated by Figure 13, where the two simulations, with and without oxidation, are compared. Both the plateaux after heating up and cooling down are well captured with the values of recombination coefficient $\gamma_r = 0.6$ ($\gamma_r = 1$ being full recombination). An oxidation probability close to unity is in line with the works of Genge (2016) and Capek & Borovička (2017).

6. Conclusions

We present two experiments carried out in the VKI ICP wind tunnel on AB and OC samples using a methodology to reproduce flight conditions, originally developed for spacecraft applications. At surface temperatures between 2280 and 2360 K we did not observe substantial mass loss of the OC due to evaporation or mechanical removal, although melting and boiling were present. Frothing of the surface appeared to be more heterogeneous for the AB than for the OC.

Exothermic oxidation reactions of iron may play an important role in the surface chemistry. This was first inferred from the change of color of the sample after the experiment but is additionally supported by analysis of the recovered material. Finally, our synthetic model, based on a 1D heat balance in order to match the experimental surface temperature, required a contribution to the chemical heat flux by iron oxidation reactions.

Ionized atoms (Ca II, Mg II, and Fe II) were identified by emission spectroscopy in both cases of AB and OC samples, with the lines of Ca II being the strongest in the range from 350 to 450 nm.

In addition, recorded sodium and potassium emission signals could not be fully assigned to ablation of the test samples because of the use of a cork sample holder, which contaminated the boundary layer with those elements. Ideally, a pure basalt/chondrite sample in the test shape (hemisphere) is suggested.

For future modeling of such experiments we suggest a comparison with a material code coupled to a flow solver. This would allow a better comparison of the experimental data, for example, the species evolution in the boundary layer, or the internal thermal response of the test sample if thermocouples are being used inside the sample.

Our experiments, together with petrography and geochemistry of the recovered material presented in an accompanying paper, demonstrate the successful use of a ground-test facility to reproduce the atmospheric entry conditions likely to be encountered by meteoroids. This paves the way for intensified analysis of meteor data by comparing ground-tested materials with collected meteorites and, therefore, may help to better characterize the composition and origin of meteors.

The research of F.B. is funded by a PhD grant of the Research Foundation Flanders (FWO) and that of B.D. by a PhD grant of the Funds for Research Training in Industry and Agriculture (FRIA). The Plasmatron experiments were sponsored by the Belgian Science Policy Office (BELSPO), under the Belgian Research Action through Interdisciplinary Networks (BRAIN) funding CONTRAT BR/143/A2/METRO. Nadine Mattielli of the Université Libre de Bruxelles is thanked for providing the basalt used as the meteorite analog.

ORCID iDs

Bernd Helber https://orcid.org/0000-0002-0700-2610
Bruno Dias https://orcid.org/0000-0002-2468-2769
Federico Bariselli https://orcid.org/0000-0002-5169-9793
Lidia Pittarello https://orcid.org/0000-0002-1080-0226
Steven Goderis https://orcid.org/0000-0002-6666-7153
Seann J. McKibbin https://orcid.org/0000-0001-5046-9358

References

Agrawal, P., Jenniskens, P. M., Stern, E., Arnold, J., & Chen, Y.-K. 2018, in Aerodynamic Measurement Technology and Ground Testing Conf. (Reston, VA: AIAA) , 4284
Allen, H. J., & Baldwin, B. S., Jr. 1967, JGR, 72, 3483
Anderson, J. D. J. 1989, Hypersonic and High Temperature Gas Dynamics (New York: McGraw-Hill)
Barbante, P., & Chazot, O. 2006, JTHT, 20, 493
Barbante, P., Degrez, G., & Sarma, G. 2002, JTHT, 16, 490
Blanchard, M. B., & Cunningham, G. G. 1974, JGR, 79, 3973
Bones, D. L., Gómez Martín, J. C., Empson, C. J., et al. 2016, RScI, 87, 094504
Borovička, J., Koten, P., Spurný, P., & Štork, R. 2008, EM&P, 102, 485
Borovička, J., & Spurný, P. 1996, Icar, 121, 484
Borovička, J., Spurný, P., Brown, P., et al. 2013, Natur, 503, 235
Bottin, B. 1999, PhD thesis, Université de Liège, von Karman Institute for Fluid Dynamics
Bottin, B., Chazot, O., Carbonaro, M., van der Haegen, V., & Paris, S. 1999, in RTO AVT Course on Measurement Techniques for High Enthalpy and Plasma Flows, RTO EN-8 (Rhode-Saint-Genèse: VKI)
Bronshten, V. A. 1983, Physics of Meteoric Phenomena (Dordrecht: Reidel)
Brown, P. G., Assink, J. D., Astiz, L., et al. 2013, Natur, 503, 235
Campbell-Brown, M. D., Borovička, J., Brown, P. G., & Stokan, E. 2013, A&A, 557, A41
Capek, D., & Borovička, J. 2017, P&SS, 143, 159
Consolmagno, G. J., Schaefer, M. W., Schaefer, B. E., et al. 2013, P&SS, 87, 146
Degrez, G., Vanden Abeele, D. P., Barbante, P. F., & Bottin, B. 2004, Int. J. Numer. Meth. Heat. Fluid Flow, 14, 538
Eppelbaum, L., Kutasov, I., & Pilchin, A. 2014, Thermal Properties of Rocks and Density of Fluids (Berlin: Springer), 99
Fay, J., & Riddell, F. 1958, Journal of the Aeronautical Sciences, 25, 73
Ferus, M., Koukal, J., Lenža, L., et al. 2018, A&A, 610, A73
Flynn, G. J. 2002, in Extraterrestrial Dust in the Near-Earth Environment, ed. E. Murad & I. P. Williams (Cambridge: Cambridge Univ. Press), 77
Genge, M. J. 2016, M&PS, 51, 1063
Gómez Martín, J. C., Bones, D. L., Carrillo Sánchez, J. D. A. D. J., et al. 2017, ApJ, 836, 212
Hardy, T. L., & Nakanishi, S. 1984, Cathode Degradation and Erosion in High Pressure Arc Discharges, Tech. Rep. NASA TM-83638, Lewis Research Center, Cleveland, Ohio
Helber, B., Asma, C. O., Babou, Y., et al. 2014, JMatS, 49, 4530
Helber, B., Chazot, O., Hubin, A., & Magin, T. 2015, Compo, 72, 96
Helber, B., Chazot, O., Hubin, A., & Magin, T. E. 2016a, J. Vis. Exp., 112, e53742
Helber, B., Turchi, A., Scoggins, J. B., Hubin, A., & Magin, T. E. 2016b, IJHMT, 100, 810
Jacchia, L. G., & Whipple, F. L. 1961, SCoA, 4, 97
Jarosewich, E. 1990, Metic, 25, 323
Kojitani, H., & Akaogi, M. 1995, GeoRL, 22, 2329
Kolesnikov, A. F. 1993, FlDyR, 28, 131
Lodders, K. 2003, ApJ, 591, 1220
Loehle, S., Zander, F., Hermann, T., et al. 2017, ApJ, 837, 112
Love, S. G., & Brownlee, D. E. 1993, Sci, 262, 550
Magin, T. E., & Degrez, G. 2004, JCoPh, 198, 424
Martínez Picar, A., Marqué, C., Verbeeck, C., et al. 2016, in Proc. Int. Meteor Conf., ed. A. Roggemans & P. Roggemans (Egmond: WGN), 175
Milley, E. P., Hawkes, R. L., & Ehrman, J. M. 2007, MNRAS, 382, L67
Pittarello, L., Goderis, S., Soens, B., et al. 2019, Icar, in press
Prabhu, D. K., Agrawal, P., Allen, G. A. J., et al. 2015, 4th IAA Planetary Defense Conf. (Frascati: ESA ESRIN), 15
Shepard, C. E., Stine, H. A., Vorreiter, J. W., & Winovich, W. 1967, A Study of Artificial Meteors as Ablators, NASA Tech. Note D-3740
Taylor, M. G. G. T., Altobelli, N., Buratti, B. J., & Choukroun, M. 2017, RSPTA, 375, 20160262
Thomas, R. N., & White, W. C. 1953, ApJ, 118, 555
Turchi, A., Matesanz, S., Juan, J., Magin, T. E., & Chazot, O. 2015, 8th European Symp. on Aerothermodynamics for Space Vehicles (Lisbon: ESA ESTEC)
Vanden Abeele, D., & Degrez, G. 2000, AIAAJ, 38, 234
Vernazza, P., Zanda, B., Nakamura, T., Scott, E. R. D., & Russell, S. 2015, in The Formation and Evolution of Ordinary Chondrite Parent Bodies, ed. P. Michel, F. E. DeMeo, & W. F. Bottke (Tucson, AZ: Univ. Arizona Press), 617
Vilas, F. 2008, AJ, 135, 1101
Vondrak, T., Plane, J. M. C., Broadley, S., & Janches, D. 2008, ACP, 8, 7015
White, S. M., & Stern, E. 2017, in 80th Annual Meeting of The Meteoritical Society (Santa Fe, NM: LPI), 6130
Yomogida, K., & Matsui, T. 1983, JGR, 88, 9513
Zotikov, I. A. 1962, Experimental Investigation of the Ablation of Bodies by Hypersonic Flow, Tech. Rep. N71-71474, NASA